

Article

# Experimental Study of CO<sub>2</sub>-Water-Mineral Interactions and Their Influence on the Permeability of Coking Coal and Implications for CO<sub>2</sub>-ECBM

Hui Guo <sup>1,2</sup> , Xiaoming Ni <sup>3</sup>, Yanbin Wang <sup>4</sup>, Xiaomin Du <sup>1</sup>, Tengteng Yu <sup>4</sup> and Ruimin Feng <sup>5,\*</sup> 

<sup>1</sup> Development and Research Center of China Geological Survey, Beijing 100037, China; guohui117@126.com (H.G.); dxiaomin@mail.cgs.gov.cn (X.D.)

<sup>2</sup> School of Energy Resources, China University of Geosciences, Beijing 100083, China

<sup>3</sup> School of Energy Science and Engineering, Henan Polytechnic University, Jiaozuo 454000, China; nxm1979@126.com

<sup>4</sup> College of Geoscience and Surveying Engineering, China University of Mining & Technology, Beijing 100083, China; wyb@cumt.edu.cn (Y.W.); yutt1214@126.com (T.Y.)

<sup>5</sup> Department of Chemical and Petroleum Engineering, University of Calgary, Calgary, AB T2N 1N4, Canada

\* Correspondence: ruimin.feng@ucalgary.ca; Tel.: +1-587-575-3439

Received: 18 January 2018; Accepted: 14 March 2018; Published: 19 March 2018

**Abstract:** Coal permeability is one of the most critical parameters affecting gas flow behavior during coalbed methane (CBM) production. However, little research has been conducted on how permeability evolves after CO<sub>2</sub> injection in coking coal. Hence, examining possible chemical interactions between coal minerals, water, and injected CO<sub>2</sub> can be very helpful to better characterize coking coal. In this study, coking coal specimens obtained from the Malan and Tunlan mines located in the Gujiao block of the Qinshui basin were treated with water and CO<sub>2</sub> to achieve a better understanding of their dissolution kinetics, pore structure, and permeability. It was found that the relative carbonate mineral content decreases with time, while the relative clay mineral content increases after the reaction with CO<sub>2</sub> and water. Scanning electron microscopy (SEM) confirmed these mineral alteration phenomena. Carbonate minerals (calcite, dolomite) dissolve faster than clay minerals (montmorillonite, illite and kaolinite). In particular, the dissolution rates of Ca<sup>2+</sup> in carbonate minerals increases with decreasing temperature (25–45 °C) and pH (4.3–6.3), and the dissolution rate of Ca<sup>2+</sup> ions in the calcite reaction solution is higher than that in the dolomite solution. In addition, the results of low-pressure nitrogen adsorption analysis showed that CO<sub>2</sub> injection can enlarge smaller size pores into larger size pores and change the overall pore size distribution. Therefore, CO<sub>2</sub> injection can increase the porosity of coal beds and ultimately their permeability, which in turn facilitates CBM production.

**Keywords:** CO<sub>2</sub> injection; ion dissolution; reaction kinetics; pore structure; coal permeability

## 1. Introduction

Owing to the increasing demand for clean energy and shortage of conventional oil and gas resources, China has started actively looking for alternative energy sources [1]. Coal-bed methane (CBM) represents a highly efficient source of clean energy and is considered an important promoter of the energy production and consumption revolution in China. However, low permeability of coal bed reservoirs in China is a major challenge faced by the CBM industry, leading to a low yield of the existing CBM wells [2–4]. Various permeability enhancement techniques such as hydraulic fracturing, nitrogen foam fracturing, and methane displacement by CO<sub>2</sub> have been employed to promote

transport of CBM and increase its recovery rate [5–7]. Among these methods, the CO<sub>2</sub>-enhanced CBM recovery (CO<sub>2</sub>-ECBM) technique not only enables the geological storage of CO<sub>2</sub> gas (which can reduce greenhouse gas emissions), but also optimizes the CBM recovery process, leading to significant economic and environmental benefits. The very first CO<sub>2</sub>-ECBM studies were conducted by American researchers. For example, the reservoir simulations performed at the Allison Unit ECBM Pilot in San Juan confirmed the improvement of the CBM recovery rate and sequestration of a large quantity of CO<sub>2</sub> in a coalbed formation [8]. Afterwards, the CO<sub>2</sub>-ECBM method was used in China, and the pilot trial in the anthracite region of the southern Qingshui basin has laid a solid foundation for conducting more extensive future field tests [9].

Since CO<sub>2</sub> exhibits a higher absorption capacity as compared to that of methane, many research groups have performed extensive experimental studies on the methane displacement by CO<sub>2</sub> injection and found that CO<sub>2</sub> adsorption induced coal matrix swelling can lead to permeability reduction even though a higher gas production can be achieved. However, CO<sub>2</sub> injection into water-saturated coal formation before primary gas production would also change the structure of the coal seam. Dissolution of mineral occlusions in coking coal seams with highly mineralized fractures is expected to considerably influence fluid flow capacities, since high-ash coal reservoirs with low permeability often contain considerable amounts of clay minerals, carbonate minerals, pyrite, and quartz, which tend to fill up the pores and cracks of the coal bed. Fluid seepage mainly occurs through natural cleats or fractures, the interaction of minerals with CO<sub>2</sub> and groundwater significantly affects the flow characteristics of coal reservoirs [10]. Various studies on the mechanism of CO<sub>2</sub>-water-rock interactions have been conducted [11–14], the role of acidification to rock minerals through CO<sub>2</sub> injection, with the huge potential for CO<sub>2</sub> storage, was identified in saline aquifers and depleted oil and gas reservoirs. Considering its successful use in the oil and gas extraction industry, the acidizing approach was utilized for CBM recovery. During CO<sub>2</sub>-ECBM, injection of CO<sub>2</sub> into the coal bed formations produces a weakly acidic fluid due to the reaction with mining water [15]. At specific pressure and temperature, chemical reactions occurred on the surface of coal minerals (Table 1). During the early stage of CO<sub>2</sub> injection, chemical reactions may result in the dissolution of carbonate minerals; however, the increase in the pH of the system can also lead to re-precipitation of carbonate minerals. Kaolinite, montmorillonite, and illite minerals are relatively stable in acidic solutions; however, they can also block the pores for fluid flow in coal reservoirs. The presence of these minerals in carbonate solutions (which will be discussed in detail in the subsequent sections) affects permeability of coal reservoirs, but very few research studies on the impact produced by the mineral chemistry on the permeability of coal reservoirs have been conducted up to date.

**Table 1.** Chemical reactions of various minerals in carbonic acid in the initial reaction period.

Reaction	Mineral	Equation
Dissolution	Calcite	$\text{CO}_2 + \text{H}_2\text{O} + \text{CaCO}_3 = \text{Ca}(\text{HCO}_3)_2$
	Dolomite	$\text{CaMg}(\text{CO}_3)_2 + 2\text{CO}_2 + 2\text{H}_2\text{O} = \text{Ca}(\text{HCO}_3)_2 + \text{Mg}(\text{HCO}_3)_2$
Precipitation	Chlorite	$[\text{Fe}/\text{Mg}]_5\text{Al}_2\text{Si}_3\text{O}_{10}(\text{OH})_8 + 5\text{CaCO}_3 + 5\text{CO}_2 = 5\text{Ca}[\text{Fe}/\text{Mg}](\text{CO}_3)_2 + \text{Al}_2\text{Si}_2\text{O}_5(\text{OH})_4 + \text{SiO}_2 + 2\text{H}_2\text{O}$
	Potassium feldspar	$2\text{KAlSi}_3\text{O}_8 + 2\text{CO}_2 + 3\text{H}_2\text{O} = 2\text{KHCO}_3 + 4\text{SiO}_2 + \text{Al}_2\text{Si}_2\text{H}_4\text{O}_9$

Interaction of minerals in the coal matrix with CO<sub>2</sub> and water can affect pore size distribution and permeability [16], and is directly related to the production and utilization of CBM. Previous coal acidification experiments revealed that the injection of supercritical CO<sub>2</sub> can lead to dissolution of some organic compounds in the coal matrix, which significantly increased the fraction of pores and fractures and thus enhance the coal permeability [17]. It has been reported that, during the simulation of the CO<sub>2</sub> storage process in the underground coal bed of a high-pressure supercritical CO<sub>2</sub> geochemical reactor, the influence of the CO<sub>2</sub> injection on the permeability of medium rank coal mainly depended on the presence of meso- and macropores [18,19].

In recent years, utilization of CBM obtained from the coking coal reservoirs in China has made rapid progress. However, the majority of the CO<sub>2</sub>-ECBM-related studies were focused either on

high-rank or low-rank coal areas, while very little attention was paid to the improvement of the permeability of medium rank coal via CO<sub>2</sub> injection (especially for the coking coal region of the Gujiao block located in the northwestern Qinshui basin). As one of the main production sites of coking coal in China, the Gujiao block of the Xishan coal field in Shanxi has been transformed into a commercial exploitation area for CBM; therefore, its exploration can be performed for both scientific and commercial purposes.

In this work, the influence of the CO<sub>2</sub> injection on the permeability of medium rank coal has been investigated from a chemical perspective in order to further increase CBM production in the coking coal regions of the Malan and Tunlan mines. In particular, changes in ion concentrations in the reaction solution were examined after mineral transformations, and reaction kinetics simulations were conducted for the main minerals to discuss the effects of the mineral chemistry on the pore size distribution and permeability of the coal matrix, providing experimental support for the CO<sub>2</sub>-ECBM technology.

## 2. Experimental Methodology

The tested coal samples were retrieved from coal seam #3 of the lower Triassic Shanxi formation in the Malan and Tunlan coal mines. Both mines are located in the Gujiao block of the Xishan coalfield in the northwestern Qinshui basin of Shanxi Province, China (Figure 1). Before the beginning of the experiments, all samples were oven-dried at a temperature of 110 °C for 12 h.

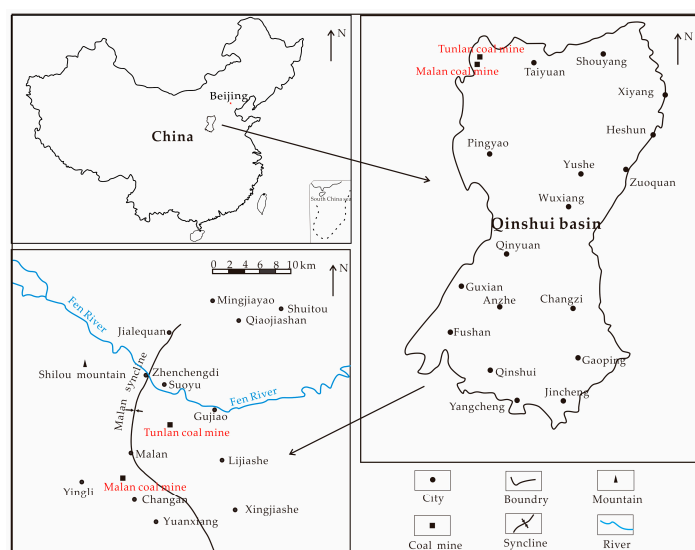
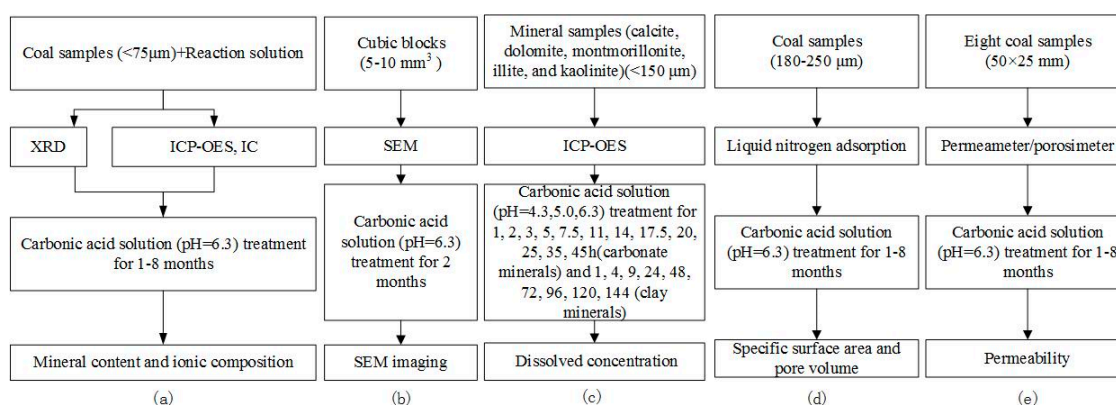


Figure 1. Location of sampling area.

To simulate the weakly acidic fluid formed by the dissolution of CO<sub>2</sub> in mine water, reaction solutions were prepared from dry ice and distilled water. Six different types of experiments were conducted in this study following the procedures described in Figure 2. (1) X-ray diffraction (XRD) measurements were performed to determine the mineral compositions of the coal samples before and after CO<sub>2</sub> injection; (2) During the acidification stage, the content of each ion type was affected by the reaction between the solid coal and the solution, therefore, the concentration of each ion in solution was measured before and after treatment; (3) To investigate the pore structures of the coal samples before and after acidification, scanning electron microscopy (SEM) studies was conducted. (4) To determine which particular mineral plays a prominent role in the chemical reaction at different stages, the reaction rate and time required to reach equilibrium were measured for each mineral under various temperature and pressure conditions; (5) Specific surface areas, pore volumes, and pore diameter distributions of the tested samples were measured/calculated at different times during acidification by

performing low-pressure nitrogen gas adsorption studies; (6) Permeability tests were performed by conducting fluid flooding experiments at different stages of the acidification process.



**Figure 2.** Scheme of acidification experiments and the techniques used in this study. (a) Measurement of mineral content and ionic composition of coal samples and reaction solution; (b) Coal samples were used to in-situ observation of dissolution structure; (c) Measurement of dissolved concentration performed on mineral samples (e.g., calcite, dolomite, montmorillonite, illite and kaolinite); (d) Measurement of specific surface area and pore volume performed on coal samples; (e) Eight coal samples used for permeability measurement.

### 2.1. Mineral Composition and Ion Content

The coal samples were ground into particles with diameters less than 200 mesh (<75 µm) before XRD (Bruker, Rheinstetten, Germany) tests. The detailed experiment methods and principles were given in prior publication [20]. Table 2 lists the mineral compositions before acidification, indicating relatively high contents of clay minerals (illite, montmorillonite, and kaolinite), which were equal to 93% for Malan coal and 85% for Tunlan coal. In contrast, the corresponding contents of carbonate minerals (calcite, dolomite) were very low, 3% for Malan coal and 6% for Tunlan coal, respectively.

All ion content measurements were conducted, the preliminary results obtained for the water sample are listed in Table 3. The concentrations of positive ions in the reaction solution were determined via inductively coupled plasma atomic emission spectroscopy (ICP-OES) (Varian, Palo Alto, CA, USA). The concentrations of negative ions were tested by ion chromatography (IC).

**Table 2.** Mineral composition of coal samples.

Sample	wt %								
	Kaolinite	Illite	Chlorite	Montmorillonite	Quartz	Potassium Feldspar	Calcite	Dolomite	Hematite
Malan	16.5	45.3	1.9	29.3	1	3	0	3	0
Tunlan	34.1	31.6	2.6	16.7	2	2	2	4	5

**Table 3.** The preliminary result of water sample.

Items	pH	Positive Ion (mg/L)				Negative Ion (mg/L)			
		K <sup>+</sup> + Na <sup>+</sup>	Mg <sup>2+</sup>	Ca <sup>2+</sup>	Total Content	HCO <sub>3</sub> <sup>-</sup>	SO <sub>4</sub> <sup>2-</sup>	Cl <sup>-</sup>	Total Content
Ion content	7.12	23.05	7.32	2.65	33.02	86.62	1.03	1.89	89.54

### 2.2. Scanning Electron Microscopy

To study the microstructure of coals before and after CO<sub>2</sub> and water treatment (pH = 6.3, reaction period of two months), SEM was employed to acquire the superficial morphological features of the samples. The coal samples were crushed into 5–10 mm<sup>3</sup> size blocks, and flat surface zones were marked as inspection regions. A Hitachi S-3400 (Hitachi, Tokyo, Japan) was used for the SEM experiments. Samples were then coated with gold for SEM imaging, and not used for other tests any more.

### 2.3. Mineral Reaction Kinetic Studies

Owing to the existence of mutual reactions between the carbonate minerals, water, and CO<sub>2</sub> and relatively high content of clay minerals (85–93%) in the coal samples, mineral reaction kinetic experiments were conducted for the calcite, dolomite, kaolinite, illite, and montmorillonite components. To compare the results obtained for different minerals, the concentrations of Mg<sup>2+</sup> and Ca<sup>2+</sup> ions of carbonate minerals, and Si<sup>4+</sup> and Al<sup>3+</sup> ions of the clay minerals were measured, using an inductively coupled plasma atomic emission spectroscopy (ICP-OES) technique.

To achieve high accuracy for all tests, the purity of all minerals was greater than 90%. The samples were crushed into grains of 100 mesh size, and their individual amounts were 2.0 g. Different reaction solutions with pH values of 4.3, 5.0, and 6.3 were prepared from dry ice and distilled water. Mineral samples were placed into each reaction vessel followed by the addition of 30 mL of the reaction solution and then removed after specified intervals to filter out the supernatant. Finally, the contents of Ca<sup>2+</sup>, Al<sup>3+</sup>, Mg<sup>2+</sup>, and Si<sup>4+</sup> ions in the supernatant were determined. To ensure sufficient accuracy of the experiment and subsequent analysis, each set of tests were repeated at least three times.

The ion dissolution rate under various conditions can be calculated using the following equation:

$$P_x = \frac{c_x \cdot v}{m_x} \times 100\% \quad (1)$$

where  $P_x$  is the dissolution rate of the tested ion,  $c_x$  is the mass concentration of the tested ion dissolved in the reaction solution (mg/L),  $v$  is the volume of the reaction solution (L); and  $m_x$  is the initial mass of the tested element in the solid sample (mg).

### 2.4. Low-Pressure Nitrogen Gas Adsorption Studies

The coal was ground and sieved to obtain a sample size of 60–80 mesh. Specific surface area and pore size of the coal samples were measured using the Micromeritics ASAP 2020 analyzer (Micromeritics, Minneapolis, MN, USA) located at the China University of Geosciences (Beijing, China). Testing was performed by following the protocols described in the “Determination of the specific surface area of solids by gas adsorption using the BET method” (GB/T 19587-2004) [21] and “Pore size distribution and porosity of solid materials by mercury porosimetry and gas adsorption-Part 2: Analysis of mesopores and macropores by gas adsorption” (GB/T 21650.2-2008) [22] publications. Nitrogen physisorption on material surface was investigated by measuring relative pressure  $P/P_0$ , where  $P$  was the partial pressure of nitrogen, and  $P_0$  was its saturated vapor pressure at a temperature of 77 K. Adsorption-desorption curves were recorded for all samples at relative pressures of 0.01–0.99 and temperature of 77 K [23]. To remove moisture and volatile species from the coal samples, the samples were degassed at a temperature of 120 °C under vacuum for 6 h prior to the experiment. The total pore volume, specific surface area, and pore size distribution were obtained via the low-pressure nitrogen gas adsorption measurements. At a  $P/P_0$  of 0.99, the total pore volume of the studied sample was calculated by converting the total volume of the adsorbed gas into the volume of a liquid. At  $P/P_0$  values of 0.05–0.35, the measured adsorption volumes were in good agreement with Brunauer-Emmett-Teller (BET) equation [24], which was utilized for the determination of specific surface areas [25]. Micropore volumes and external surface areas (including those of mesopores and macropores) were estimated from the corresponding t-plots [26], and the specific surface areas of micropores were obtained by subtracting the related external surface areas. At  $P/P_0 \geq 0.4$ , capillary condensation occurred, and the resulting adsorption volume (related to the size of surface micropores) was estimated using Barrett-Joyner-Halenda (BJH) method.

In this study, the specific surface area, pore volume, and pore size distribution obtained at different times during the reaction between the coal samples and the corresponding solutions were analyzed to discuss the changes in the pore structure observed before and after acidification.

### 2.5. Permeability Testing

To perform permeability tests, the cylindrical core samples with diameter of 25 mm, and length of 50 mm were obtained from the corresponding coal sample beds by drilling. Four different samples (named ML 1 to ML4 and TL1 to TL4; ML refers to the Malan coal sample, TL refers to the Tunlan coal sample) were made for each coal type. The coal samples were placed in inert reaction vessels with the equivalent volumes of solution (pH = 6.3) after adding dry ice under constant temperature and pressure conditions. The permeability of each coal sample was tested every 30 days, and the entire experiment lasted for 8 months.

A pressure pulse-decay method was used to measure the permeability of the coal samples in this study. The minimum in situ horizontal stress and pore pressure were 800 psi and 600 psi, respectively, which were provided by the operators in this area, both of which were maintained during the course of experiments. At this point, the excess pressure produced relatively minor effects on the test results. The sample permeability ( $k$ ) was calculated using the following equations [27]:

$$\frac{\Delta P(t)}{\Delta P_i} = \exp(-\alpha t) \quad (2)$$

$$\alpha = \frac{kA}{\mu\beta L} \left( \frac{1}{V_u} + \frac{1}{V_d} \right) \quad (3)$$

where  $\Delta P(t)$  is the pressure difference between upstream and downstream reservoirs;  $\Delta P_i$  is the pressure difference between upstream and downstream reservoirs at initial condition;  $t$  is the time taken during each pressure step;  $k$  is the permeability;  $\mu$  is fluid viscosity at test condition;  $\beta$  is fluid compressibility;  $L$  is the sample length;  $A$  is the sample cross-section area;  $\alpha$  is the slope of the line obtained when natural logarithm of the ratio of pressure change to initial pressure difference against time at different pressures is plotted; and  $V_u$  and  $V_d$  are the volumes of the up and down-stream reservoirs.

## 3. Results

### 3.1. Ion Content

CO<sub>2</sub> injection was accompanied by the changes of the ion concentrations in the reaction solution. To investigate possible reactions of the major minerals in the coal samples, the corresponding variations of the main ions in solution (K<sup>+</sup>, Na<sup>+</sup>, Ca<sup>2+</sup>, Mg<sup>2+</sup>, HCO<sub>3</sub><sup>-</sup>, and CO<sub>3</sub><sup>2-</sup>) were measured (Figure 3). The concentrations of K<sup>+</sup> and Na<sup>+</sup> ions in the reaction solutions of the Malan coal samples increased with time from the initial value of 23.05 mg/L to 78.82 mg/L, while the concentrations of Ca<sup>2+</sup> ions initially increased and then decreased, reaching a peak value of 4.89 mg/L after 2 months of reaction after the reaction with CO<sub>2</sub>-water. The overall changes in Mg<sup>2+</sup> concentration were similar to those of Ca<sup>2+</sup> ions, reaching a peak value of 14.58 mg/L after 2 months. Among the studied anions, changes in HCO<sub>3</sub><sup>-</sup> concentration were greater than those in CO<sub>3</sub><sup>2-</sup> concentration, while both parameters exhibited an initial increase followed by a decrease. HCO<sub>3</sub><sup>-</sup> content reached its largest value after 1 month of reaction.

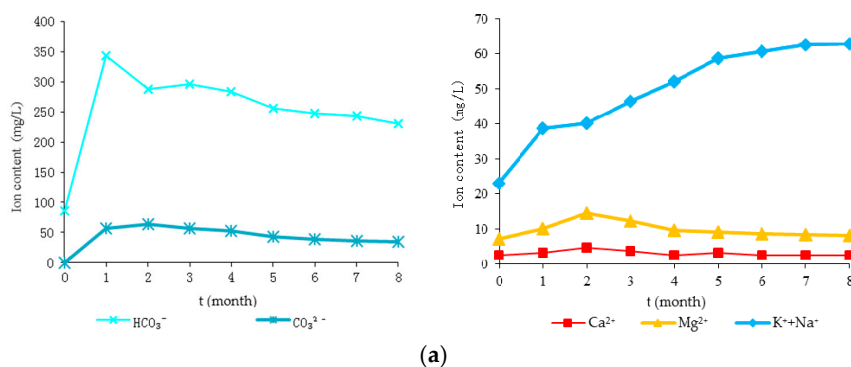


Figure 3. Cont.

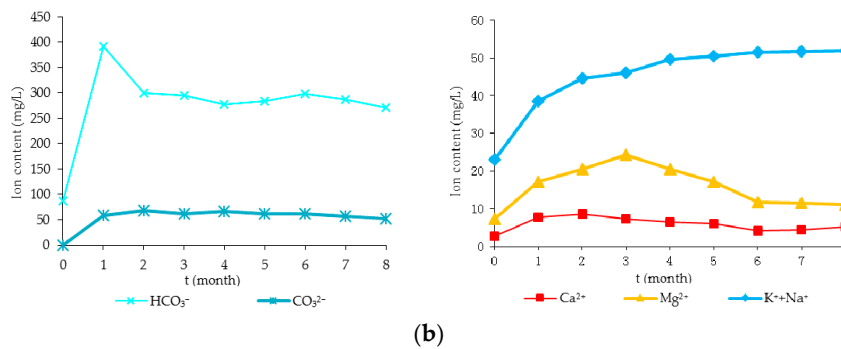


Figure 3. Variations of ion contents with time: (a) ML and (b) TL.

The variations of ion contents in the reaction solutions of Tunlan coal samples were similar to those observed for Malan coal samples. However, the corresponding concentrations of  $\text{Ca}^{2+}$ ,  $\text{Mg}^{2+}$ ,  $\text{HCO}_3^-$ , and  $\text{CO}_3^{2-}$  ions were higher for Tunlan coal samples. In contrast, the concentrations of  $\text{K}^+$  and  $\text{Na}^+$  ions in the reaction solution of for Tunlan coal samples were lower than those for Malan coal samples.

### 3.2. Mineral Composition

To examine changes in the mineral compositions of the coal samples during acidification, their mineral contents were analyzed by X-ray diffraction (XRD) at different acidification stages (Figure 4). In Figure 4a, the relative content of dolomite species decreases with time from the initial value of 3 wt % to 0.6 wt %. The observed changes in the potassium feldspar content (from 3 wt % to 0.8 wt %) are consistent with those in the dolomite concentration, while the variations of the relative clay content were not significant, corresponding to the increase from the initial value of 93 wt % to 95 wt %. Among the studied clay minerals, the relative content of kaolinite increased from the initial value of 16.5 wt % to 21.4 wt % and then decreased to 20.3 wt % after the completion of the experiment. The variations of the chlorite, illite, and montmorillonite contents were relatively small, while the relative concentration of quartz increased from 1 wt % to 3.6 wt %. The trends observed for the contents of clay minerals, quartz, potassium feldspar, and dolomite in the Tunlan coal samples were similar to those determined for the Malan coal samples (thus, the relative content of calcite in the Tunlan coal samples decreased from 2 wt % to 0.2 wt %).

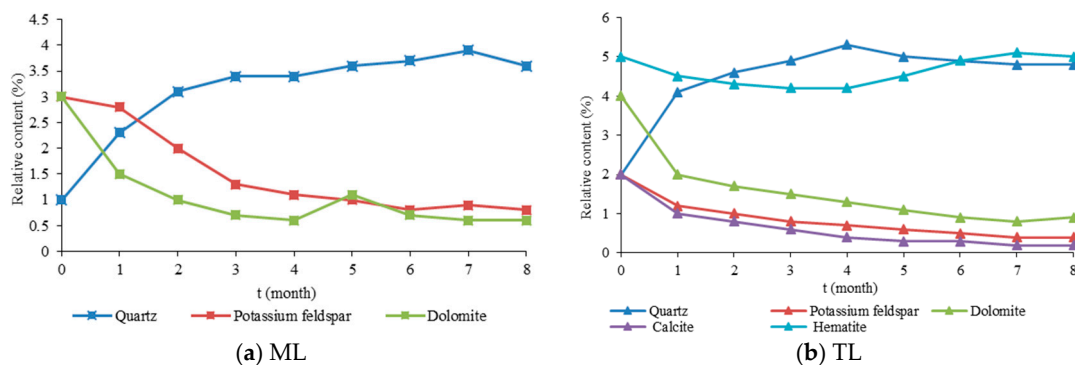
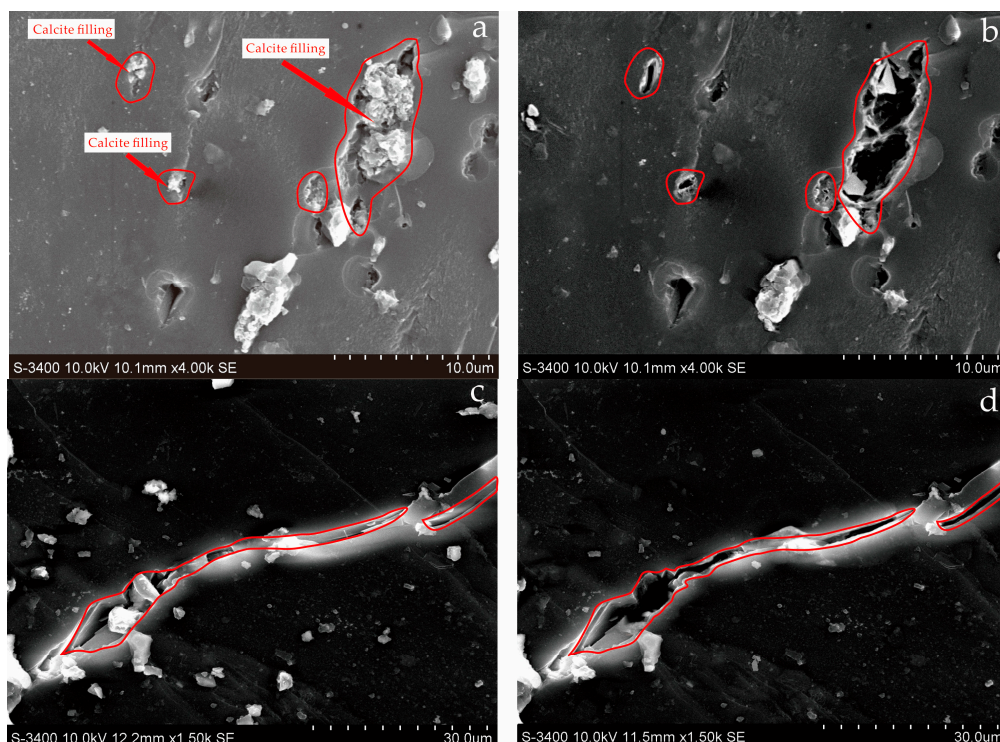


Figure 4. Variations of mineral contents with time: (a) ML and (b) TL.

### 3.3. Variable Features of Pores and Microfractures

To visualise the effect of  $\text{CO}_2$  and water on microstructure of coal, a series of SEM images were taken from the surface of treated coal. Partial microfracture ( $>1 \mu\text{m}$ ) images of coal samples before and after acidification obtained using SEM are presented in Figure 5. The pores and microfractures

in the treated specimens were extended, multiplied than those in the initial coal samples. It could be demonstrated that acidification led to an increase in the average pore size and number of pores and microfractures. More minerals were dissolved to some extents in the pores and microfractures in the raw specimens. A similar result has been observed by Wen et al. [28] upon mineral dissolution and removal by CO<sub>2</sub> treatment, with pore volume enlarged naturally.



**Figure 5.** SEM images of untreated (a,c) and treated (b,d) coal samples. (a,b) present nano-scale pores on the surface of coal matrix before and after treatment; (c,d) present natural fractures before and after treatment.

### 3.4. Dissolution Rates of Ion

The dissolution rates measured under different temperature and pH conditions for various ions of calcite, dolomite, montmorillonite, illite and kaolinite minerals are shown in Figure 6. It was found that the dissolution rates of Ca<sup>2+</sup>, Mg<sup>2+</sup>, and Si<sup>4+</sup> present an obvious fluctuation with time, while the dissolution rate of Al<sup>3+</sup> fluctuates only slightly without showing any distinct pattern.

During the interaction of calcite and dolomite with the reaction solution, the dissolution rate of Ca<sup>2+</sup> was stabilized after around 40 h. In the solution with the pH value of 4.3, the peak values of the dissolution rate of Ca<sup>2+</sup> ion in the calcite and dolomite solutions were 0.53–0.60% and 0.44–0.49%, respectively. In the solution with the pH value of 5, these values were in the range of 0.48–0.55% and 0.36–0.41%, while for the solution with the pH of 6.3, their ranges were 0.39–0.42% and 0.30–0.34%, respectively. According to the results presented in Figure 6a,b, the dissolution rate of Ca<sup>2+</sup> in the calcite reaction solution was higher than that in the dolomite solution, and the former system reached the average peak value earlier, indicating that calcite dissolved in the reaction solution faster than dolomite. Under different pH conditions, the dissolution rate of Ca<sup>2+</sup> ions in the calcite and dolomite solutions decreased with increasing temperature. As shown in Figure 6c, consistent variations of the Mg<sup>2+</sup> concentration were observed for the dolomite solutions prepared under different conditions. In particular, for all these systems, the dissolution rate reached maximum after around 11 h followed by a distinct turning point after 17.5 h of reaction. Overall, the dissolution rate of Mg<sup>2+</sup> decreased with

an increase in pH value; however, it was slightly affected by temperature variations. The amount of dissolved  $Mg^{2+}$  ions in the dolomite reaction mixture was smaller than that of  $Ca^{2+}$ .

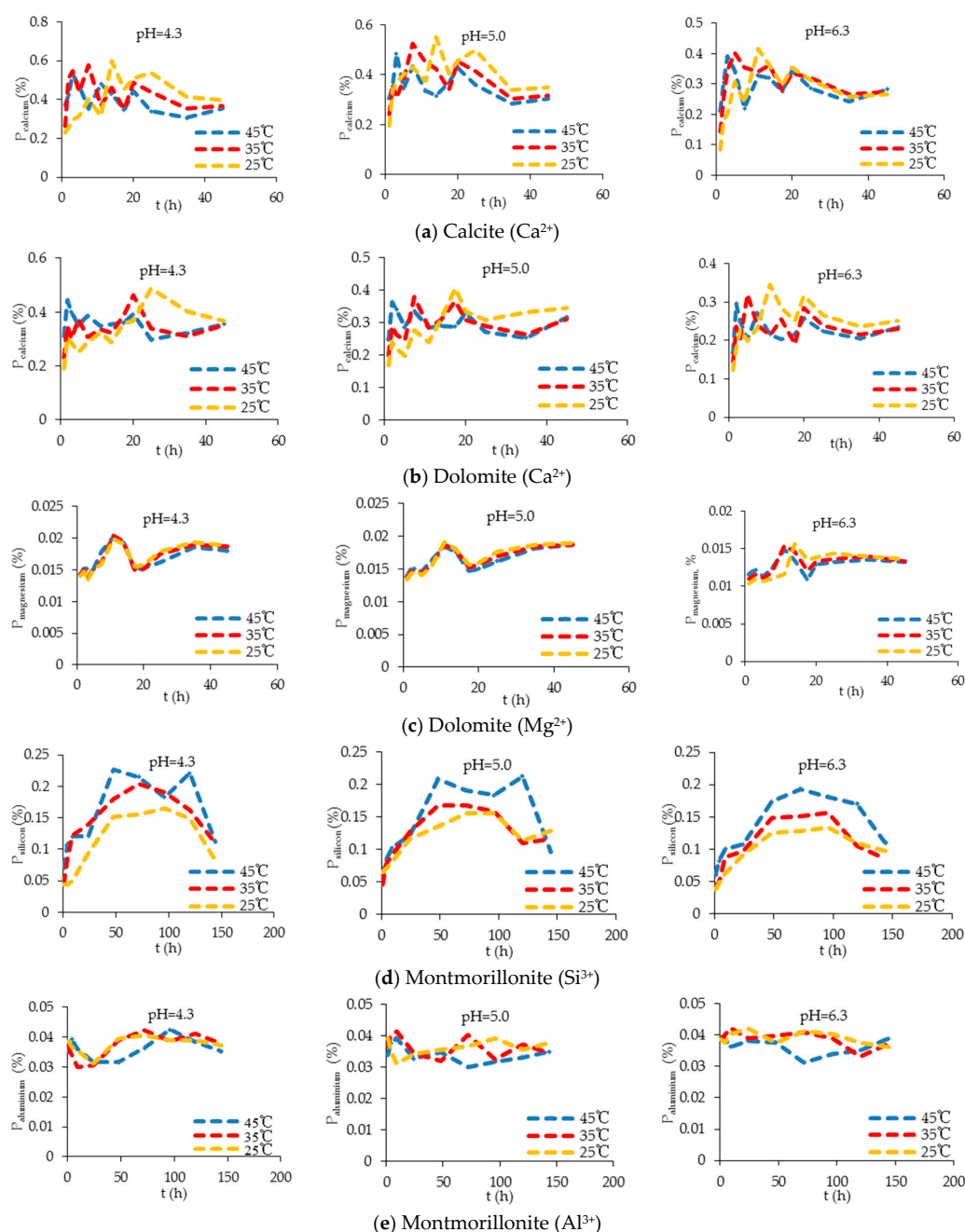


**Figure 6.** Dissolving-out ratio (P)-time profiles for dissolutions of calcite (a), dolomite (b,c), montmorillonite (d,e) in respective reaction solutions under different temperatures and pH values. Among clay minerals, montmorillonite was taken as an example in this figure, because of the similarity with the laws of ion dissolution rate curve in montmorillonite, illite and kaolinite.

The dissolution rate of  $Si^{4+}$  ion in the reaction solutions of montmorillonite, illite, and kaolinite increased with increasing temperature regardless of pH values of the solutions (Figure 6). At different temperatures, the silicon dissolution rate increased with decreasing pH value. The higher was the temperature, the shorter was the time required to reach the peak dissolution rate; hence, the dissolution rate of  $Si^{4+}$  ions reached maximum faster than those of the other ions at the highest experimental temperature of 45 °C. However, no distinct pattern can be observed from changes in the dissolution

rate of  $\text{Al}^{3+}$  ions. Among the three clay minerals, the dissolution rate of  $\text{Si}^{4+}$  followed the order of montmorillonite > illite > kaolinite. In particular, the dissolution rate of  $\text{Si}^{4+}$  in the montmorillonite reaction solution reached the peak value of 0.25% at a pH value of 4.3 and temperature of 45 °C.

### 3.5. Changes in Specific Surface Area and Pore Volume

Currently, there are various pore classification standards existing, in which the classification recommended by International Union of pure and Applied Chemistry (IUPAC) is. Pore size can be divided into three types: macropores (>50 nm), mesopores (2–50 nm), and micropores (<2 nm) [29,30]. The macropores and mesopores are responsible for seepage and gas flow, while the micropores participate in the adsorption process and are used for the storage of gas species.

#### 3.5.1. Variations of Specific Surface Area and Pore Volume

As shown in Table 4, the BET specific surface areas of the Malan and Tunlan coal samples before acidification measured via low-pressure nitrogen gas ( $\text{N}_2$ ) adsorption are 0.41  $\text{m}^2/\text{g}$  and 0.53  $\text{m}^2/\text{g}$ , respectively. According to the obtained t-plot, their external specific surface areas are equal to 0.34  $\text{m}^2/\text{g}$ , and the micropore specific surface areas were 0.07 and 0.19  $\text{m}^2/\text{g}$ , respectively. The total pore volumes estimated for the Malan and Tunlan coal samples are 0.0024  $\text{cm}^3/\text{g}$  and 0.0019  $\text{cm}^3/\text{g}$ , while the corresponding micropore volumes are equal to 0.000043  $\text{cm}^3/\text{g}$  and 0.000106  $\text{cm}^3/\text{g}$ , respectively. In addition, Table 4 also shows that the micropore specific surface areas of the Malan and Tunlan coal samples amounted to 17.07% and 35.85% of their respective BET specific surface areas, and their micropore volumes are equal to 2.39% and 5.58% of the corresponding total pore volumes, suggesting that the presence of micropores more significantly contributes to the specific surface area of coal than to its total pore volume, and that the specific surface area depends on the micropore size [31]. As a result, smaller average pore diameters produced larger specific surface areas.

**Table 4.** Specific surface area and pore volume of Malan and Tunlan samples before treating.

Samples	Specific Surface Area <sup>a</sup> , $\text{m}^2/\text{g}$	$S_{\text{ext}}$ <sup>b</sup>	$S_{\text{mic}}$ <sup>c</sup> , $\text{m}^2/\text{g}$	Specific Surface Area Contributed by Micropores, %	Total Pore Volume <sup>d</sup> , $\text{cm}^3/\text{g}$	$V_{\text{mic}}$ <sup>e</sup> , $\text{cm}^3/\text{g}$	Total Pore Volume Contributed by Micropores, %	Average Pore Size <sup>f</sup> , nm
Malan	0.41	0.34	0.07	17.07	0.0018	0.000043	2.39	17.66
Tunlan	0.53	0.34	0.19	35.85	0.0019	0.000106	5.58	14.58

<sup>a</sup> Specific surface area was calculated by the BET method; <sup>b</sup>  $S_{\text{ext}}$ , the surface area of mesopores, macropores and other external specific surface area; <sup>c</sup>  $S_{\text{mic}}$ , the surface area of the micropores; <sup>d</sup> Total pore volume was estimated to be the liquid volume of nitrogen at a relative pressure of 0.99; <sup>e</sup>  $V_{\text{mic}}$ , the micropore volume; <sup>f</sup> Average pore size =  $4 \times$  total pore volume/specific surface area.

The specific surface area and pore volume of Malan and Tunlan coal samples demonstrated certain changing patterns after eight months of acidification. As shown in Figure 7, their magnitudes increases first and then decreases, exhibiting some fluctuations. Thus, the BET specific surface area and total pore volume measured for the Malan coal sample reached the maximum values of 0.51  $\text{m}^2/\text{g}$  and 0.0025  $\text{cm}^3/\text{g}$  after six months of acidification with the corresponding rates of change equal to 30% and 40%, respectively. The Tunlan coal sample reaches its maximum BET specific surface area and total pore volume of 0.73  $\text{m}^2/\text{g}$  and 0.0029  $\text{cm}^3/\text{g}$  after five months of acidification (the corresponding rates of change were 73% and 54%, respectively).

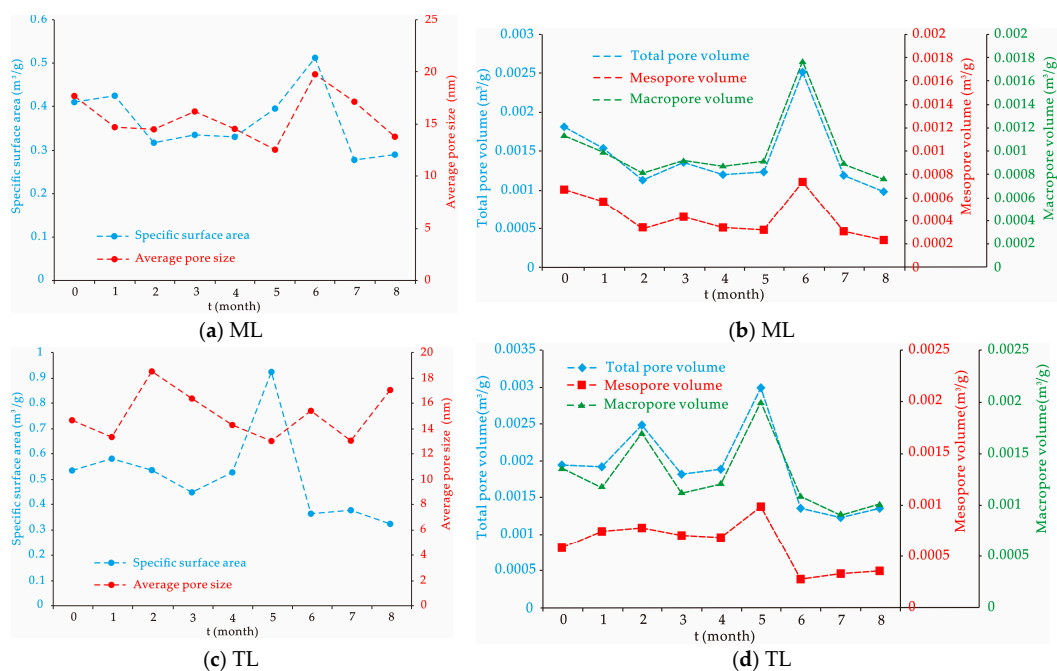


**Figure 7.** Dynamic of specific surface area (a,c) and pore volume (b,d) over time. ML represents Malan samples and TL represents Tunlan samples. Specific surface area was calculated through the BET method. Mesopore volume was calculated using the BJH method.

### 3.5.2. Variations of Pore Size Distribution

Since a certain amount of micropores turned into other pores during acidification, their changes were not taken into account during the analysis of the pore size distribution of the studied samples. Thus, the Barrett-Joyner-Halenda (BJH) method was used to analyze the pore size distributions of the mesopores and macropores for Malan and Tunlan coal samples during acidification [31,32]. According to Figure 8 the pore size distributions of the Malan and Tunlan coal samples before acidification exhibit single peaks in the range of 70–90 nm, indicating a relatively high content of large pores. After four months of the reaction of the Malan coal sample with the acid solution, its pore size distribution starts to exhibit two peaks centered at 2–3 nm and 80–90 nm. Similarly, after three months of the reaction of the Tunlan coal sample with the acid solution, its pore size distribution also begins to show two peaks at 2–3 nm and 80–100 nm. The Malan and Tunlan coal samples reach their maximum numbers of mesopores and macropores after six and five months of acidification reaction, respectively, which were subsequently decreased upon further treatment.

### 3.6. Variation of Coal Permeability

The variation of coal permeability with time was measured to evaluate the effect of the chemical reaction on the coal fracture. The main physical parameter measured during simulations was the coal permeability, which served as an important indicator of the pore connectivity and fracture and was able to characterize the migration of CMB species in the coal seam. After permeability testing, the coal permeability increases and then decreases with time, exhibiting some fluctuations, as shown in Figure 9. By fitting the permeability data obtained for the coal samples, it can be shown that the Malan sample reached its maximum permeability (corresponding to an average value of around  $0.28 \times 10^{-3} \mu\text{m}^2$ ) after approximately 7.2 months of acidification. Similarly, the Tunlan coal sample reached its maximum permeability corresponding to an average value of  $0.87 \times 10^{-3} \mu\text{m}^2$  after about 7.5 months of acidification. The obtained results indicate that while both the Malan and Tunlan coal samples reached the maximum permeability at around the same time, but their corresponding magnitudes were significantly different. As shown in Figure 9, although permeability of the Malan

and Tunlan coal samples decrease after almost 7 months of acidification, the final permeability is still greater than the initial permeability. This means the permeability can be enhanced ultimately.

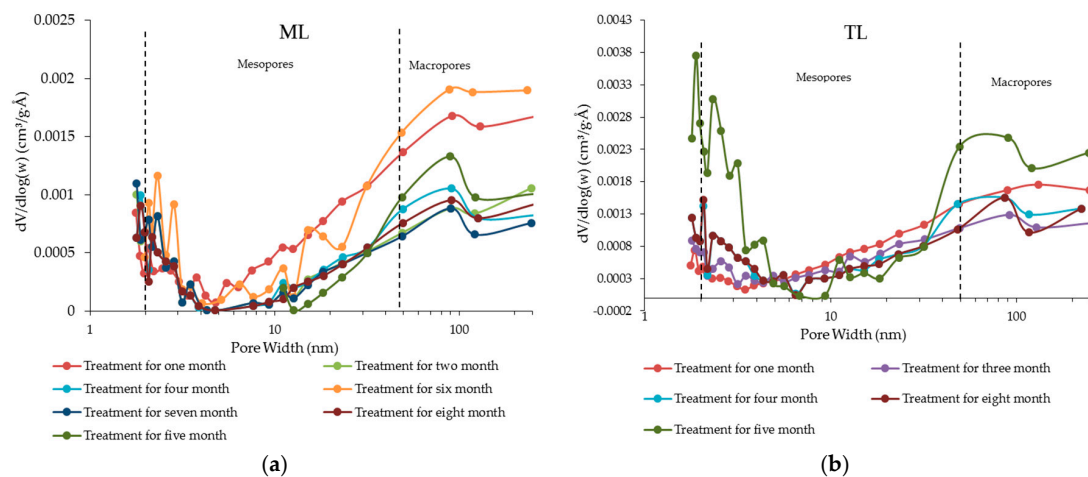


Figure 8. Distributions of BJH pore size for Malan (ML) and Tunlan (TL) samples before and after treatment: (a) ML and (b) TL.

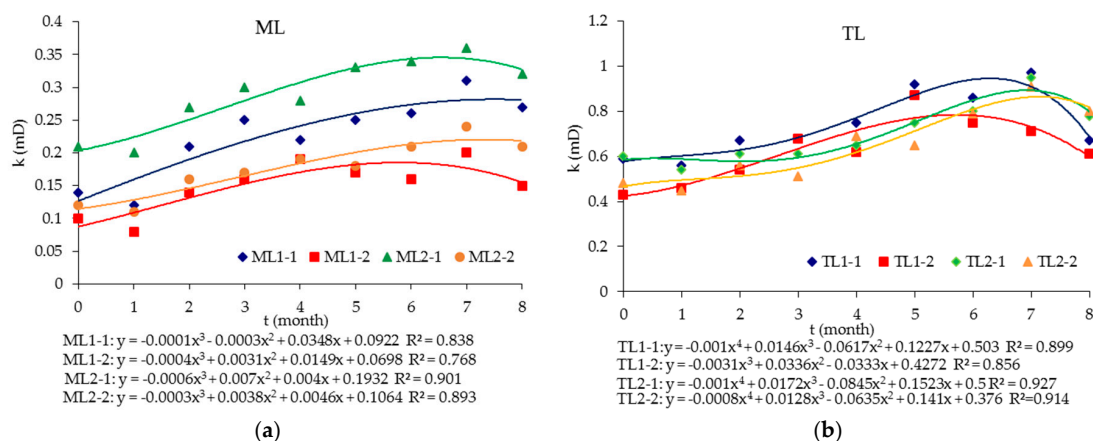


Figure 9. Permeability changes of Malan (ML) and Tunlan (TL) samples over time. The fitting formulas below dictate the permeability trends of all the samples: (a) ML and (b) TL.

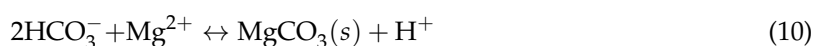
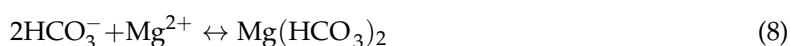
## 4. Discussion

### 4.1. Variation Analysis of Ion Content Dissolution Rates

#### 4.1.1. Variation of Ion Content

CO<sub>2</sub> takes part in a series of chemical reactions and greatly influences mineral composition and ion content. HCO<sub>3</sub><sup>-</sup> and CO<sub>3</sub><sup>2-</sup> concentration firstly increases, then decreases with time in Figure 3a,b. Once CO<sub>2</sub> is injected, it reacted to form carbonic acid. But carbonic acid (H<sub>2</sub>CO<sub>3</sub>) is unstable in water solution, and decomposes to form H<sup>+</sup> and HCO<sub>3</sub><sup>-</sup> (Equations (4) and (5)). Meanwhile HCO<sub>3</sub><sup>-</sup> decomposed into H<sup>+</sup> and CO<sub>3</sub><sup>2-</sup> (Equation (6)). HCO<sub>3</sub><sup>-</sup> combined with positive ion in water solution as shown in Equations (7) and (8). Subsequently, bicarbonate and carbonate ions collided with divalent cation, they formed carbonate (Equations (9–12)). Their precipitation is generally considered to be the main way for CO<sub>2</sub> mineral storage. In the entire experimental system, the observed changes of Ca<sup>2+</sup> can be mainly attributed to the reactivity of dolomite mineral [CaMg(CO<sub>3</sub>)<sub>2</sub>]. During the initial stages, the interaction between dolomite and CO<sub>2</sub> species occurred, which resulted in a continuous increase

in the concentration of  $\text{Ca}^{2+}$  ions and formation of bicarbonate ions. Subsequently, the interaction between soluble bicarbonate and  $\text{Ca}^{2+}$  ions led to the precipitation of calcium carbonate and continuous decrease in  $\text{Ca}^{2+}$  content (Equation (9)).  $\text{Mg}^{2+}$  were mainly supplied by dolomite [ $\text{CaMg}(\text{CO}_3)_2$ ] and chlorite [ $\text{Mg}_{2.5}\text{Fe}_{2.5}\text{Al}_2\text{Si}_3\text{O}_{10}(\text{OH})_8$ ] species. Since the reaction solution contains large amounts of  $\text{CO}_3^{2-}$  and  $\text{HCO}_3^-$  ions, leading to precipitation of  $\text{Mg}^{2+}$  ion and thus decrease in its concentration in the solution.  $\text{K}^+$  and  $\text{Na}^+$  mainly originated from potassium feldspar and illite minerals. They had similar chemical nature, and no precipitate is produced in acidic and alkaline conditions. Their content was determined by reaction process, therefore, gradually increased with time. The concentrations of  $\text{Ca}^{2+}$ ,  $\text{Mg}^{2+}$ ,  $\text{HCO}_3^-$ , and  $\text{CO}_3^{2-}$  ions were higher for Tunlan coal samples due to their larger fraction of carbonate minerals, which exhibited higher reactivity toward acids. Among these ions, the increase in the concentration of  $\text{Ca}^{2+}$  species resulted from the presence of both dolomite and calcite ( $\text{CaCO}_3$ ) minerals. The contents of potassium feldspar and illite minerals in Tunlan coal samples were relatively small, so the concentrations of  $\text{K}^+$  and  $\text{Na}^+$  ions in the reaction solution of Tunlan coal samples were lower:



#### 4.1.2. Ion Dissolution of the Pure Minerals

##### Variation Analysis of Dissolution Rates

In the reaction process of the pure carbonate minerals (calcite and dolomite), the dissolution rate of  $\text{Ca}^{2+}$ ,  $\text{Mg}^{2+}$  firstly increases and then decreases due to the dissolution reaction (Figure 6a–c). But they are balanced in later stage reaction, which can be attributed to the depletion of  $\text{H}^+$  species. Owing to the exothermic nature of the carbonate mineral dissolution process and related inhibition of this reaction at higher temperatures, the dissolution rate of  $\text{Ca}^{2+}$  ions in the carbonate minerals solutions decreased with increasing temperature. During the reaction, the time required to reach the maximum dissolution rate decreased with increasing temperature due to the increase in the reaction rate at higher temperatures. Regardless of the reaction temperature, the dissolution rate was inversely proportional to the solution's pH value. There was a distinct turning point after 17.5 h of the  $\text{Mg}^{2+}$  concentration, which could be due to the formation of  $\text{MgCO}_3$  precipitate. The amount of dissolved  $\text{Mg}^{2+}$  ions in the dolomite reaction mixture was smaller than that of  $\text{Ca}^{2+}$ , which was due to the greater atomic mass of  $\text{Ca}^{2+}$  as compared to that of  $\text{Mg}^{2+}$ , and the number of ions were the same.

The dissolution rate of  $\text{Si}^{4+}$  ion in the reaction solutions of montmorillonite, illite, and kaolinite firstly increased and then decreased (Figure 6d). After the maximum, the formation of  $\text{Si}(\text{OH})_4$  colloidal precipitate inhibited the dissolution of  $\text{Si}^{4+}$ . However, there is no distinct rule in the dissolution rate of  $\text{Al}^{3+}$  (Figure 6e), indicating the absence of  $\text{Al}^{3+}$  precipitation. Among the clay minerals, the dissolution rate of  $\text{Si}^{4+}$ , in order of the content, were montmorillonite, illite, kaolinite, indicating a relatively high ion exchange capacity of the mineral. The crystal structure of montmorillonite is that of a 2:1-type layered silicate with each layer unit consisting of two silicon-oxygen tetrahedra and one

aluminum-oxygen octahedron in the center (the interaction between its different layers occurs via weak intermolecular forces). Owing to the isomorphous substitution of cations with different valences in the layered montmorillonite structure, the resulting permanent negative charges are able to attract cations located between its layers, leading to a high cation exchange capacity. Kaolinite is a 1:1-type layered aluminum silicate, which contains crystal layers connected via hydrogen bonds; as a result, water molecules are unable to penetrate multiple kaolinite layers easily. Illite corresponds to a 2:1-type layered clay mineral with the apical oxygens of the silicon-oxygen tetrahedra pointing toward the aluminum-oxygen octahedra. These two structures are connected via their shared oxygen atoms to form tightly bonded crystal layers that do not allow easy penetration of water molecules. Hence, different chemical properties of montmorillonite, illite, and kaolinite minerals are related to their crystal structures.

### Kinetic Models

To predict which mineral played a dominant role in the experimental procedure, a set of reaction kinetic equations were utilized to elucidate the effect produced by these parameters on the mineral chemistry.

#### (1) Carbonate minerals

The chemical reactions during carbonate dissolution are usually described as three parallel processes occurring at the mineral/water interface [33], and the overall dissolution rate ( $r$ , 5–60 °C) can be expressed using the following formula [33–36]:

$$r = k_1 \cdot a_{\text{H}^+} + k_2 \cdot a_{\text{CO}_2} + k_3 \cdot a_{\text{H}_2\text{O}} - k_4 \cdot a_{\text{Ca}^{2+}} \cdot a_{\text{HCO}_3^-} \quad (13)$$

where  $j$  is the index representing Ca/Mg,  $a_i$  is the activity of aqueous species, and  $k_i$  is the rate constant measured at a particular temperature. Constants of  $k_1$ ,  $k_2$  and  $k_3$  are used to characterize the kinetics of the positive (dissolution) reaction (for calcite,  $k_1 = 10^{(0.198-444.0/T_K)}$  and  $k_2 = 10^{(2.84-2177.0/T_K)}$ ). When the reaction temperature is less than or equal to 25 °C,  $k_3 = 10^{(-5.86-317.0/T_K)}$ , while at higher temperatures. The constant  $k_4$  is used to describe the reverse reaction,  $k_4 = 1 - \left(\frac{\text{IAP}}{K_{\text{calcite}}}\right)^{\frac{2}{3}}$  (Here IAP represents the ion activity product, and  $K_{\text{calcite}}$  is the solubility product of calcite).

Because the Phreeqc software uses Equation (13) for simulating the dissolution rate of calcite, the same program has been successfully utilized for modeling its reaction kinetics. Since calcite is a carbonate mineral, its dissolution reaction is exothermic. During the dissolution of calcite, its saturation index increases with temperature, while the observed increase in the rate of calcium dissolution become slower, indicating that higher temperatures do not favor the dissolution of minerals (Figure 10). In addition, higher reaction temperatures results in an earlier chemical equilibrium, lower saturation index, and smaller quantity of the calcite reactant.

Furthermore, at the temperature of 25 °C and CO<sub>2</sub> partial pressure of 1 atm, the saturation index remains greater than 0, while the content of calcium ions decreases, indicating a precipitation reaction (Figure 11). After the CO<sub>2</sub> partial pressure was raised to 50 atm, the saturation index decreased to a magnitude below 0 (which corresponds to a dissolution reaction) and reaches a constant level with time. When the CO<sub>2</sub> partial pressure exceeds the liquefaction point, the presence of CO<sub>2</sub> molecules begin to inhibit the dissolution reaction. Therefore, the optimum CO<sub>2</sub> partial pressure for the dissolution reaction of carbonate minerals is located slightly below the liquefaction point.

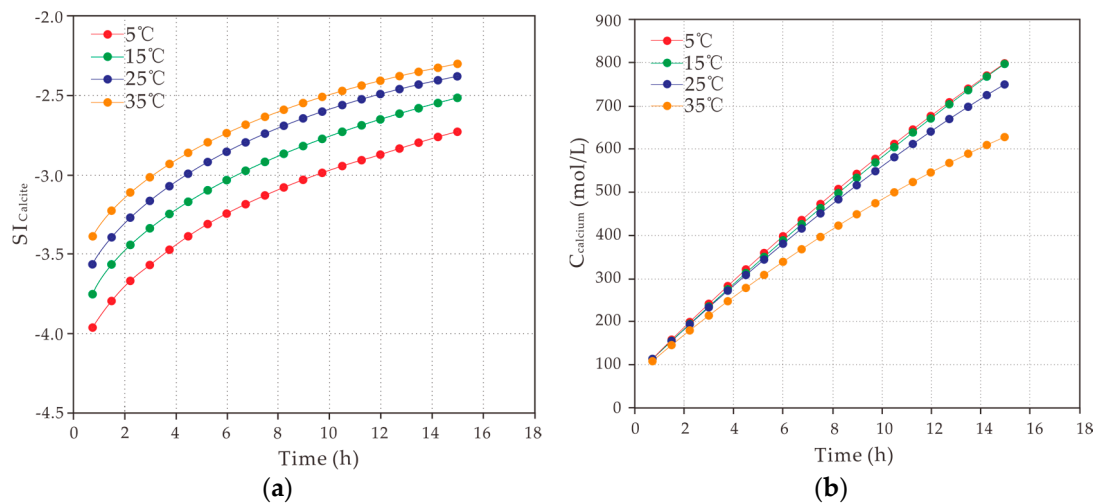


**Figure 10.** Saturation indexes (SI) for concentration of calcite and calcium at different temperatures: (a)  $SI_{calcite}$  and (b)  $C_{calcium}$ .

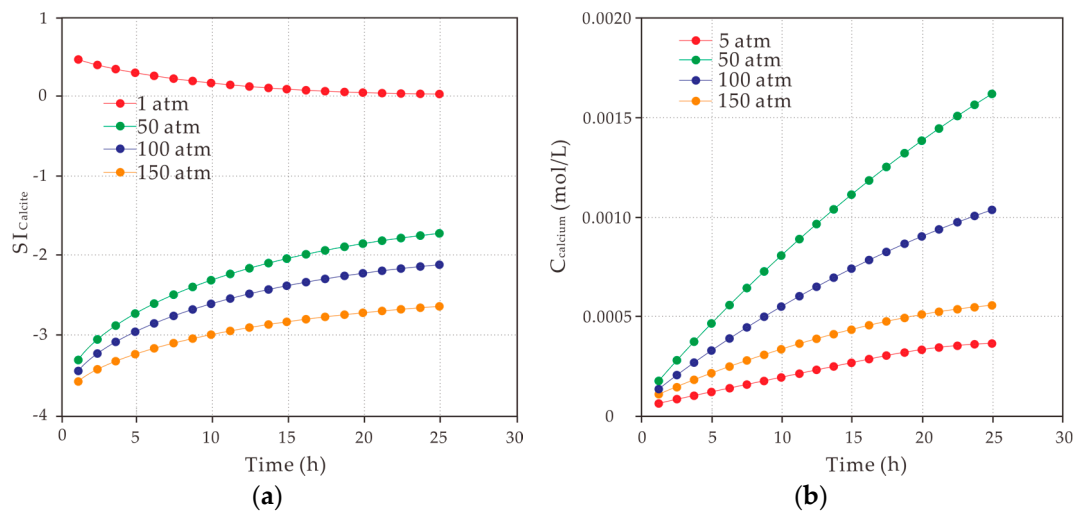


**Figure 11.** Saturation indexes (SI) for concentrations of calcite and calcium at different pressures: (a)  $SI_{calcite}$  and (b)  $C_{calcium}$ .

(2) Clay minerals

Since the most prominent pattern was observed for the silicon dissolution in the montmorillonite, illite, and kaolinite reaction solutions, its kinetic characteristics were analyzed to obtain the corresponding reaction kinetic equation (its total rate could be determined from the diffusion rate of Si cations and chemical reaction rate). Because the related diffusion mechanism has not been clarified yet, the main kinetic parameters were obtained via model fitting. Five different models (including the first-order and second-order reaction equations, chemical reaction-controlled model, interfacial diffusion-controlled model, and two-dimensional internal diffusion-controlled model) were selected to investigate the acid dissolution of the studied minerals. To determine the most suitable kinetic model, their applicability for fitting the values of the experimentally obtained apparent activation energies were examined.

The apparent activation energy of a process is usually determined using the Arrhenius equation [37,38], which can be written in the following form:

$$\ln k = [\ln A - E/(RT)] \tag{14}$$

where  $k$  is the reaction rate constant,  $T$  is the temperature (in K),  $R$  is the molar gas constant equal to  $8.314472 \text{ J}/(\text{mol}\cdot\text{K})$ ,  $E$  is the activation energy (in J), and  $A$  is the pre-exponential factor, which is equal to  $k$  at  $T \rightarrow \infty$ .

Thus, the activation energy  $E$  can be estimated by plotting  $\ln k$  as a function of  $1/T$ . In general, the reactions with apparent activation energies higher than  $42.0 \text{ kJ}\cdot\text{mol}^{-1}$  are considered to be controlled by the chemical reaction (otherwise, they represent diffusion-controlled reactions). The resulting values of the apparent activation energy exhibits relatively large differences. Both the first- and second-order reaction equations as well as the chemical reaction-controlled model do not produce satisfactory fitting results; however, the interfacial diffusion-controlled and two-dimensional internal diffusion-controlled models are able to meet the expectations (Table 5). Since the interfacial diffusion-controlled model produced a better fitting, it was further utilized as the kinetic model for montmorillonite, kaolinite, and illite minerals. The obtained results indicate that at lower temperatures, the measured reaction rate constants were smaller, and the corresponding reaction processes were slower. At lower pH, the reaction activation energy was lower, which led to more effective molecular collisions during ionic exchange and, therefore, higher reaction rates.

**Table 5.** Fitting constants and apparent activation energies by using interfacial diffusion-controlled model for montmorillonite <sup>a</sup>.

Models	Items	Temperature			Ea, $\text{kJ}\cdot\text{mol}^{-1}$	Judgement Value of Ea, $\text{kJ}\cdot\text{mol}^{-1}$	If the Results Meet the Adopted Model	
		25 °C	35 °C	45 °C				
Interfacial diffusion-controlled model $1 - 3(1 - X)^{2/3} + 2(1 - X)$	pH = 4.3	$k(10^{-12})$	3.59	5.09	6.23	21.79	<42.0	Yes
		$R^2$	0.95	0.95	0.86			
	pH = 5.0	$k(10^{-12})$	2.87	3.77	5.23	23.63	<42.0	Yes
		$R^2$	0.96	0.91	0.85			
	pH = 6.3	$k(10^{-12})$	1.79	2.45	3.46	25.97	<42.0	Yes
		$R^2$	0.91	0.89	0.88			
	$R^2$	-	-	-				

<sup>a</sup> Montmorillonite was taken as an example in this table, because of the similarity of kinetic models for montmorillonite, illite and kaolinite.

#### 4.2. Variation of Mineral Composition

By analyzing the changes in the concentrations of ions, it was found that a few amount of minerals were dissolved and precipitated; and also, there were new minerals formed due to ion exchange with the carbonic acid solution produced by  $\text{CO}_2$  injection. Changes of the ion concentrations in the reaction solution of the studied coal samples with time was accompanied by transformation of the mineral components. As shown in Figure 4, the relative content of carbonate minerals (dolomite and calcite) decreases with time, which could be attributed to the dissolution reaction of carbonate minerals with  $\text{CO}_2$  and water. But the relative content of dolomite increased after 5 months' reaction. Since the solution gradually becomes alkaline during the acidizing process, the  $\text{Ca}(\text{HCO}_3)_2$  species produced from the interaction of dolomite with  $\text{CO}_2$  and water reprecipitates in the form of  $\text{CaCO}_3$  particles. The relative content of potassium feldspar decreased during the whole process, it could be concluded that the ion exchange and mineral composition conversion could occur. The relative content of kaolinite increased, which could be attributed to the formation of new kaolinite and quartz species due to the reaction of potassium feldspar with  $\text{CO}_2$  and water. Because of the relatively weak interactions of clay minerals with acids, the variations of the chlorite, illite, and montmorillonite contents were relatively small. In addition to the newly synthesized  $\text{SiO}_2$  species through the reaction of potassium feldspar with the solution (as indicated by the observed decrease in the relative contents of dolomite and potassium feldspar as well as by the relatively small contents of clay minerals with acids), quartz species, which are stable at acidic conditions, were formed.

#### 4.3. Influence of Minerals Reaction on Pore Structure

Results from variation of ions content and mineral composition evidence the presence of minerals reaction after CO<sub>2</sub> injection. The observed differences in the change of the specific surface area and pore volume of the Malan and Tunlan coal samples were mainly due to their mineral compositions, mineral reactions and pore structures. As shown in Figure 7a, the average pore sizes and specific surface areas of the studied samples exhibit opposite trends. As the average pore size decreases, the specific surface area increases, indicating the existence of a reciprocal relationship between these two parameters. Malan coal samples contained micropores before acidification, and a fair amount of them turn into mesopore after it. The micropore volume of Tunlan coal samples was reduced after one month of acidification. These changes most likely resulted from the enlargement and interaction of the adjacent micropores during acidification, leading to the formation of mesopores and macropores. The changing pattern observed for the total pore volume was identical to those for the mesopore and macropore volumes, indicating that it was mainly influenced by the presence of mesopores and macropores in the coal matrix. From Figure 7, the formation of mesopores and increase in the size of macropores were more obviously after four and three months of the acidification of the Malan and Tunlan coal samples, respectively. This phenomenon can be attributed to the reaction of carbonate minerals with the acid solution during acidification caused by their subsequent dissolution. The original micropores either increased in volume or became connected to the adjacent pores to form mesopores, while the size of the original macropores also increased due to the increase in their initial volume. In general, the pore sizes of the studied samples increased by different degrees during acidification. But in later stages, pore volume decrease due to the precipitation (Si(OH)<sub>4</sub>, CaCO<sub>3</sub>, MgCO<sub>3</sub>) which could block the pores and throat, reducing connectivity between inner pores. These results demonstrate that CO<sub>2</sub> injection increases the volume of pores, particularly macropores. Furthermore, CO<sub>2</sub> injection improved the pore size distribution, resulting in a wider range of pore sizes.

#### 4.4. Effects of CO<sub>2</sub> Injection on Coal Permeability

##### 4.4.1. Influence of Minerals Reaction on Permeability

The variation of ions content, dissolution rates and minerals composition contribute to the understanding of minerals interactions after CO<sub>2</sub> injection. From Figure 5, dissolution and precipitation of minerals due to reaction of CO<sub>2</sub>-water-minerals could be clearly observed. With the progress of the experiments, various elements released into the reaction solution from primary samples, resulting in changes in ion concentrations and corresponding minerals composition in the aqueous phase.

Their dissolution and precipitation influence the porosity and permeability of coal after CO<sub>2</sub> injection. From Figure 9, the improved results of permeability were significantly different. This phenomenon can be explained by the more superior mineral content, pore characteristics, or initial permeability of the Tunlan coal sample (as compared to those of the Malan sample), which led to its greater permeability increase after acidification.

During the early stage of acidification, montmorillonite and illite minerals rapidly expanded after water absorption, leading to the cleavage of side chains and clogging of pore channels, which reduced their permeability and produced an overall negative effect on the coal permeability change. The Si(OH)<sub>4</sub> precipitate formed during the reaction exhibited colloidal properties. Owing to its relatively large volume, even small amounts of Si(OH)<sub>4</sub> could block wide seepage channels, which impacted the coal permeability in a negative way. In addition, bicarbonate and carbonate which were formed by recrystallization also could block the pores, reducing the permeability. At the same time, the initial interaction between the samples and the carbonate solution caused the active exchange between carbonate (calcite and dolomite) minerals and ions in solution. During this time, some of the present carbonate minerals dissolved, thus interconnecting the pores and fractures of the coal matrix and increasing its permeability. This process had a positive effect on the coal permeability change.

As shown in Figure 9, after one month of acidification, permeability of the Malan and Tunlan coal samples decreased first and then gradually increased, owing to the swelling of clay minerals during the initial reaction stage followed by the dissolution of carbonate minerals, which gradually increased the coal permeability. As the carbonate species became depleted, the  $\text{Si}(\text{OH})_4$  precipitate produced during the clay mineral reaction was transported into the coal pores by fluids, leading to their blockage. The resulting negative effect thus became dominant, and the coal permeability decreased gradually. Carbonate minerals constitute up to 2% of the total rock mineral content of the Malan coal sample and up to 5% of that of the Tunlan coal sample; hence, the observed increases in the ion exchange degree and permeability were greater for the Tunlan sample. At the same time, the initial permeability of the Tunlan sample was higher than that of the Malan sample, which facilitated the penetration of the acid solution into its pores and subsequent mineral dissolution. Therefore, the Tunlan coal sample exhibited a greater increase in permeability after acidification by a factor of about 1.5 (as compared to its initial value).

Based on analyzing the reaction kinetics of pure minerals, it could be concluded that the reaction of carbonate mineral, especially, calcite plays a dominant role in the experimental procedure. Apart from dissolution of carbonate mineral on coal surfaces, dissolution of the carbonate mineral in pores and microfracture also plays a significant role in increasing in pore volume. The dissolution of carbonate mineral contribute significantly to the connectivity of pore networks. As a result, the dissolution can lead to a higher porosity and permeability of coal samples.

#### 4.4.2. Influence of Pore Structure on Permeability

Based on low-pressure nitrogen gas adsorption study, untreated coal samples contain mostly macropores and mesopores, followed by micropores. The coal samples treated with  $\text{CO}_2$  and water contains high levels of macropores and mesopores.  $\text{CO}_2$  injection altered the pore volume distribution. Specific surface area and total pore volume increased by 73% and 54% respectively after acidification. Among all types of pores, the largest increase was the mesopore volume, which rose by 70%. The macropores and mesopores are responsible for seepage and gas flow, mainly contributing to the permeability of coals. Acidification leads to mineral dissolution, as a result, altering the mineral content and the porosity. It is often considered that the pore size distribution is more important than pore volume for gas transport [39].  $\text{CO}_2$  injection changes the pore size distribution, which results in a wider range of pore sizes and an increase in pore connectivity. The improvement in pore volume and change in pore size distribution during  $\text{CO}_2$  injection facilitates coalbed methane diffusion from the coal matrix surface and thus contributes to coalbed methane transport in coal. Ultimately,  $\text{CO}_2$  injection increases the coal permeability. Mineral and structural studies provided confirmation of the geochemical simulations predicting the mineral alteration phenomena. Therefore, by altering the pore structure, permeability pathways can conduct fluids better.

### 5. Implication for $\text{CO}_2$ -ECBM

The present study was conducted to investigate the possibility of using  $\text{CO}_2$  for improving the permeability in coking coal. According to the results, injecting  $\text{CO}_2$  greatly enhances the permeability of coal samples with more carbonate mineral content, better pore characteristics, or higher initial permeability. So, mineral content, pore characteristics, initial permeability and time of  $\text{CO}_2$  injection should be considered for in-situ  $\text{CO}_2$ -ECBM projects. From the analysis of kinetic models, the best conditions to increase the dissolution rate of carbonate minerals is low temperature and high pressure which is located slightly below the liquefaction point. These conditions need to be taken into account as well.

At present,  $\text{CO}_2$  has been used for trial tests by several researchers. For example, one test was conducted in the Shizhuangbei block of the southern Qinshui basin. The SX-001 well was selected to perform field tests. The coal-bearing strata in the area include Permian Shanxi Formation ( $P_{1s}$ ), Carboniferous Taiyuan Formation ( $C_{3t}$ ). The No. 3 coal seam with thick seam and stable distribution in the whole area are main target layer in ECBM exploration, which belong to  $C_{3t}$ . The permeability

value of coal seam varies from  $0.002\text{--}0.8 \times 10^{-3} \mu\text{m}^2$  with large variations. The reservoir pressure is 2.4–6.14 MPa, the average temperature of the reservoir is 24 °C. The mineral content in coal is mainly controlled by clay minerals, with a little minerals of carbonate, sulphides and silicon oxide. Before CO<sub>2</sub> injection, the highest gas production is 169.8 m<sup>3</sup>/day with stable gas production of 80 m<sup>3</sup>/day. After CO<sub>2</sub> injection with almost five months, the highest gas production is 421 m<sup>3</sup>/day with stable gas production of 196 m<sup>3</sup>/day. The gas production is 2.45 times as high as test suggested by initial studies. It fully demonstrates that CO<sub>2</sub> injection can increase the coal-bed methane production. Meanwhile, the concentrations of K<sup>+</sup> + Na<sup>+</sup>, HCO<sub>3</sub><sup>−</sup>, Ca<sup>2+</sup>, Mg<sup>2+</sup> increased with corresponding time from the initial value of 479.64 mg/L, 110.90 mg/L, 2.81 mg/L, 1.17 mg/L to 578.35 mg/L, 973.79 mg/L, 139.36 mg/L, 14.45 mg/L, respectively. Besides, the permeability increased to a certain extent, from 5.5 mD to 20 mD, with the range of high-permeability region increasing.

However, the experiments presented in this study were performed on the certain coal samples without consideration of the in-situ stress, temperature and adsorbed gas in nanopores. These conditions may influence the acidizing effect in CO<sub>2</sub>-ECBM. The findings of this investigation can be used as a platform to implement acidification studies to determine the effect of various effective factors, and to extend knowledge about CO<sub>2</sub>-ECBM in coking coal.

## 6. Conclusions

The obtained results confirm the effect of the acidification-driven mineral changes on the permeability of medium rank coal after CO<sub>2</sub> injection. They show that the dissolution of minerals as well as their subsequent precipitation and expansibility of clay minerals first increase the coal permeability and then decrease it. From the obtained results, the following conclusions can be drawn:

- (1) After the reaction of coal samples with the carbonic acid solution, the relative carbonate mineral content decreased with time, while the relative clay mineral content increased. The contents of various ions in solution increased as well, indicating the occurrence of the ion exchange between the reaction solution and the minerals inside the coal samples.
- (2) The dissolution rates of Ca<sup>2+</sup>, Mg<sup>2+</sup>, and Si<sup>4+</sup> ions first increase and then decrease with time. The dissolution rate of Ca<sup>2+</sup> ions in calcite is higher than that in dolomite, and the dissolution rate of Mg<sup>2+</sup> ions in dolomite is smaller than that of Ca<sup>2+</sup>. The amount of silicon species dissolved in clay minerals is greater than the content of aluminum ions. The ion solubility of different clay minerals follows the order of montmorillonite > illite > kaolinite. The dissolution of Si<sup>4+</sup> ions in clay minerals can be satisfactorily described by the interfacial diffusion-controlled model, and the dissolution rate of carbonate minerals can be characterized by the Plummer formula.
- (3) As indicated by the results of low-pressure nitrogen gas (N<sub>2</sub>) adsorption, the interaction of the Malan and Tunlan coal samples with CO<sub>2</sub> and water can promote the transformation of micropores to mesopores and macropores and thus improve their pore size distributions. The BET specific surface areas and pore volumes of these samples first increase and then decrease with time. Thus, the BET specific surface area and total pore volume of the Malan coal sample reached their maximum values after six months of acidification (the corresponding rates of change were 30% and 40%, respectively). The Tunlan coal sample reached its maximum BET specific surface area and total pore volume with the corresponding rates of change of 73% and 54%, respectively, after five months of acidification.
- (4) The conducted permeability tests confirmed the increase in permeability for the Malan and Tunlan coal samples from their initial average values of  $0.14 \times 10^{-3} \mu\text{m}^2$  and  $0.56 \times 10^{-3} \mu\text{m}^2$  to  $0.28 \times 10^{-3} \mu\text{m}^2$  and  $0.86 \times 10^{-3} \mu\text{m}^2$ , respectively, owing to the dissolution of carbonate minerals, which created additional seepage channels. Since carbonate minerals constitute a larger fraction of the Tunlan coal sample, they exhibited a greater increase in permeability as compared to that of the Malan coal sample.

**Acknowledgments:** This study was supported by National Science and Technology Major Project of the Ministry of Science and Technology of China (No. 2011ZX05042-003), which was sponsored by the Ministry of Science and Technology of China. The authors would like to show their gratitude to Editage (a division of Cactus Communications) for the help of English editing and revising.

**Author Contributions:** Hui Guo, Yanbin Wang and Xiaoming Ni conceived and designed the experiments; Hui Guo performed the data analysis and wrote the Manuscript; Tengting Yu performed the experiments; Ruimin Feng performed the analysis with constructive discussions. Ruimin Feng and Xiaomin Du contributed to revising of the paper.

**Conflicts of Interest:** The authors declare no conflict of interest.

## References

1. Saghafi, A. Potential for ECBM and CO<sub>2</sub> storage in mixed gas Australian coals. *Int. J. Coal Geol.* **2010**, *82*, 240–251. [[CrossRef](#)]
2. Tian, L.; Cao, Y.; Chai, X.; Liu, T.; Feng, P.; Feng, H.; Zhou, D.; Shi, B.; Oestreich, R.; Rodvelt, G. Best practices for the determination of low-pressure/permeability coalbed methane reservoirs, Yuwu Coal Mine, Luan mining area, China. *Fuel* **2015**, *160*, 100–107. [[CrossRef](#)]
3. Wang, G.; Ren, T.; Wang, K.; Zhou, A. Improved apparent permeability models of gas flow in coal with Klinkenberg effect. *Fuel* **2014**, *128*, 53–61. [[CrossRef](#)]
4. Zhang, L.; Zhang, H.; Guo, H. A case study of gas drainage to low permeability coal seam. *Int. J. Min. Sci. Technol.* **2017**, *27*, 687–692. [[CrossRef](#)]
5. Keshavarz, A.; Badalyan, A.; Johnson, R.; Bedrikovetsky, P. Productivity enhancement by stimulation of natural fractures around a hydraulic fracture using micro-sized proppant placement. *J. Nat. Gas Sci. Eng.* **2016**, *33*, 1010–1024. [[CrossRef](#)]
6. Ranathunga, A.S.; Perera, M.S.A.; Ranjith, P.G.; Wei, C.H. An experimental investigation of applicability of CO<sub>2</sub> enhanced coal bed methane recovery to low rank coal. *Fuel* **2016**, *189*, 391–399. [[CrossRef](#)]
7. Sayyafzadeh, M.; Keshavarz, A. Optimisation of gas mixture injection for enhanced coalbed methane recovery using a parallel genetic algorithm. *J. Nat. Gas Sci. Eng.* **2016**, *33*, 942–953. [[CrossRef](#)]
8. Sayyafzadeh, M.; Keshavarz, A.; Alias, A.R.M.; Dong, K.A.; Manser, M. Investigation of varying-composition gas injection for coalbed methane recovery enhancement: A simulation-based study. *J. Nat. Gas Sci. Eng.* **2015**, *27*, 1205–1212. [[CrossRef](#)]
9. Wang, H.; Ran, Q.; Liao, X.; Zhao, X.; Xu, M.; Fang, P. Study of the CO<sub>2</sub> ECBM and sequestration in coalbed methane reservoirs with SRV. *J. Nat. Gas Sci. Eng.* **2016**, *33*, 678–686. [[CrossRef](#)]
10. Balucan, R.D.; Turner, L.G.; Steel, K.M. Acid-induced mineral alteration and its influence on the permeability and compressibility of coal. *J. Nat. Gas Sci. Eng.* **2016**, *33*, 973–987. [[CrossRef](#)]
11. Mito, S.; Xue, Z.; Ohsumi, T. Case study of geochemical reactions at the Nagaoka CO<sub>2</sub> injection site, Japan. *Int. J. Greenh. Gas Control* **2008**, *2*, 309–318. [[CrossRef](#)]
12. Varre, S.B.K.; Siriwardane, H.J.; Gondle, R.K.; Bromhal, G.S.; Chandrasekar, V.; Sams, N. Influence of geochemical processes on the geomechanical response of the overburden due to CO<sub>2</sub> storage in saline aquifers. *Int. J. Greenh. Gas Control* **2015**, *42*, 138–156. [[CrossRef](#)]
13. Yang, Q.; Matter, J.; Takahashi, T.; Stute, T.; O'Mullan, G.; Clauson, K.; Umamoto, K.; Goldberg, D. Groundwater geochemistry in bench experiments simulating CO<sub>2</sub> leakage from geological storage in the Newark Basin. *Int. J. Greenh. Gas Control* **2015**, *42*, 98–108. [[CrossRef](#)]
14. Yu, Z.; Liu, L.; Liu, K.; Yang, S.; Yang, Y. Petrological characterization and reactive transport simulation of a high-water-cut oil reservoir in the Southern Songliao Basin, Eastern China for CO<sub>2</sub> sequestration. *Int. J. Greenh. Gas Control* **2015**, *37*, 191–212. [[CrossRef](#)]
15. Cui, G.; Zhang, L.; Tan, C.; Ren, S.; Zhuang, Y.; Enechukwu, C. Injection of supercritical CO<sub>2</sub> for geothermal exploitation from sandstone and carbonate reservoirs: CO<sub>2</sub>-water-rock interactions and their effects. *J. CO<sub>2</sub> Util.* **2017**, *20*, 113–128. [[CrossRef](#)]
16. Ozdemir, E. Role of pH on CO<sub>2</sub> sequestration in coal seams. *Fuel* **2016**, *172*, 130–138. [[CrossRef](#)]
17. Hou, P.; Gao, F.; Ju, Y.; Cheng, H.; Gao, Y.; Xue, Y.; Yang, Y. Changes in pore structure and permeability of low permeability coal under pulse gas fracturing. *J. Nat. Gas Sci. Eng.* **2016**, *34*, 1017–1026. [[CrossRef](#)]
18. Liu, C.; Wang, G.X.; Sang, S.; Rudolph, V. Changes in pore structure of anthracite coal associated with CO<sub>2</sub> sequestration process. *Fuel* **2010**, *89*, 2665–2672. [[CrossRef](#)]

19. Zhang, K.; Cheng, Y.; Li, W.; Wu, D.; Liu, Z. Influence of supercritical CO<sub>2</sub> on pore structure and functional groups of coal: Implications for CO<sub>2</sub> sequestration. *J. Nat. Gas Sci. Eng.* **2017**, *40*, 288–298. [[CrossRef](#)]
20. Li, J.; Zhuang, X.; Yuan, W.; Liu, W.; Liu, B.; Querol, X.; Font, O.; Moreno, N.; Li, J.; Gang, T.; et al. Mineral composition and geochemical characteristics of the Li-Ga-rich coals in the Buertaohai-Tianjiashipan mining district, Jungar Coalfield, Inner Mongolia. *Int. J. Coal Geol.* **2016**, *167*, 157–175. [[CrossRef](#)]
21. *Determination of the Specific Surface Area of Solids by Gas Adsorption Using the BET Method*; Chinese National Standards, General Administration of Quality Supervision, Inspection and Quarantine of the People's Republic of China/Standardization Administration of the People's Republic of China: Beijing, China, 2004.
22. *Pore size Distribution and Porosity of Solid Materials by Mercury Porosimetry and Gas Adsorption*; Chinese National Standards, General Administration of Quality Supervision, Inspection and Quarantine of the People's Republic of China/Standardization Administration of the People's Republic of China: Beijing, China, 2008.
23. Xiong, J.; Liu, X.; Liang, L. Experimental study on the pore structure characteristics of the Upper Ordovician Wufeng Formation shale in the southwest portion of the Sichuan Basin, China. *J. Nat. Gas Sci. Eng.* **2015**, *22*, 530–539. [[CrossRef](#)]
24. Zhao, J.; Xu, H.; Tang, D.; Mathews, J.P.; Li, S.; Tao, S. A comparative evaluation of coal specific surface area by CO<sub>2</sub> and N<sub>2</sub> adsorption and its influence on CH<sub>4</sub> adsorption capacity at different pore sizes. *Fuel* **2016**, *183*, 420–431. [[CrossRef](#)]
25. Brunauer, S.; Emmett, P.H.; Teller, E. Adsorption of gases in multimolecular layers. *J. Am. Chem. Soc.* **1938**, *60*, 309–319. [[CrossRef](#)]
26. De Boer, J.H.; Lippens, B.C.; Linsen, B.G.; Broekhoff, J.C.P.; van den Heuvel, A.; Osinga, T.J. The t-curve of multimolecular N<sub>2</sub>-adsorption. *J. Colloid Interface Sci.* **1966**, *21*, 405–414. [[CrossRef](#)]
27. Feng, R.; Harpalani, S.; Pandey, R. Laboratory measurement of stress-dependent coal permeability using pulse-decay technique and flow modeling with gas depletion. *Fuel* **2016**, *177*, 76–86. [[CrossRef](#)]
28. Wen, H.; Li, Z.; Deng, J.; Shu, C.M.; Laiwang, B.; Wang, Q.; Ma, L. Influence on coal pore structure during liquid CO<sub>2</sub>-ECBM process for CO<sub>2</sub> utilization. *J. CO<sub>2</sub> Util.* **2017**, *21*, 543–552. [[CrossRef](#)]
29. Rouquerol, J.; Avnir, D.; Fairbridge, C.W.; Everett, D.H.; Haynes, J.H.; Pernicone, N.; Ramsay, J.D.F.; Sing, K.S.W.; Unger, K.K. Recommendations for the characterization of porous solids. *Pure Appl. Chem.* **1994**, *66*, 1739–1758. [[CrossRef](#)]
30. Sing, K.S.W. Reporting physisorption data for gas/solid systems with special reference to the determination of surface area and porosity. *Pure Appl. Chem.* **1984**, *57*, 603–619. [[CrossRef](#)]
31. Kuila, U.; Prasad, M. Specific surface area and pore-size distribution in clays and shales. *Geophys. Prospect.* **2013**, *61*, 341–362. [[CrossRef](#)]
32. Tian, H.; Pan, L.; Xiao, X.; Wilkins, R.W.T.; Meng, Z.; Huang, Z. A preliminary study on the pore characterization of Lower Silurian black shales in the Chuandong thrust fold belt, southwestern China using low pressure N<sub>2</sub> adsorption and FE-SEM methods. *Mar. Pet. Geol.* **2013**, *48*, 8–19. [[CrossRef](#)]
33. Plummer, L.N.; Wigley, T.M.L.; Parkhurst, D.L. The kinetics of calcite dissolution in CO<sub>2</sub>-water systems at 5° to 60 °C and 0.0 to 1.0 atm CO<sub>2</sub>. *Am. J. Sci.* **1978**, *278*, 179–216. [[CrossRef](#)]
34. Cheng, P.; Crawshaw, J.P.; Maitland, G.C.; Trusler, J.P.M. Kinetics of calcite dissolution in CO<sub>2</sub>-saturated water at temperatures between (323 and 373) K and pressures up to 13.8 MPa. *Chem. Geol.* **2015**, *403*, 74–85.
35. Chou, L.; Garrels, R.M.; Wollast, R. Comparative study of the kinetics and mechanisms of dissolution of carbonate minerals. *Chem. Geol.* **1989**, *78*, 269–282. [[CrossRef](#)]
36. Pokrovsky, O.S.; Golubev, S.V.; Schott, J.; Castillo, A. Calcite, dolomite and magnesite dissolution kinetics in aqueous solutions at acid to circumneutral pH, 25 to 150 °C and 1 to 55 atm pCO<sub>2</sub>: New constraints on CO<sub>2</sub> sequestration in sedimentary basins. *Chem. Geol.* **2009**, *265*, 20–32. [[CrossRef](#)]
37. Finneran, D.W.; Morse, J.W. Calcite dissolution kinetics in saline waters. *Chem. Geol.* **2009**, *268*, 137–146. [[CrossRef](#)]

38. Shi, P.; Zhang, B.; Jiang, M. Kinetics of the Carbonate Leaching for Calcium Metavanadate. *Minerals* **2016**, *6*, 102. [[CrossRef](#)]
39. Wang, H.; Fu, X.; Jian, K.; Li, T.; Luo, P. Changes in coal pore structure and permeability during N<sub>2</sub> injection. *J. Nat. Gas Sci. Eng.* **2015**, *27*, 1234–1241. [[CrossRef](#)]



© 2018 by the authors. Licensee MDPI, Basel, Switzerland. This article is an open access article distributed under the terms and conditions of the Creative Commons Attribution (CC BY) license (<http://creativecommons.org/licenses/by/4.0/>).